

Engineering nanoscale H supply chain to accelerate methanol synthesis on ZnZrO_x

Received: 13 September 2022

Accepted: 26 January 2023

Published online: 13 February 2023

Check for updates

Kyungho Lee¹, Paulo C. D. Mendes¹, Hyungmin Jeon², Yizhen Song¹, Maxim Park Dickieson¹, Uzma Anjum¹, Luwei Chen³, Tsung-Cheng Yang⁴, Chia-Min Yang^{4,5}, Minkee Choi², Sergey M. Kozlov¹✉ & Ning Yan¹✉

Metal promotion is the most widely adopted strategy for enhancing the hydrogenation functionality of an oxide catalyst. Typically, metal nanoparticles or dopants are located directly on the catalyst surface to create interfacial synergy with active sites on the oxide, but the enhancement effect may be compromised by insufficient hydrogen delivery to these sites. Here, we introduce a strategy to promote a ZnZrO_x methanol synthesis catalyst by incorporating hydrogen activation and delivery functions through optimized integration of ZnZrO_x and Pd supported on carbon nanotube (Pd/CNT). The CNT in the Pd/CNT + ZnZrO_x system delivers hydrogen activated on Pd to a broad area on the ZnZrO_x surface, with an enhancement factor of 10 compared to the conventional Pd-promoted ZnZrO_x catalyst, which only transfers hydrogen to Pd-adjacent sites. In CO₂ hydrogenation to methanol, Pd/CNT + ZnZrO_x exhibits drastically boosted activity—the highest among reported ZnZrO_x-based catalysts—and excellent stability over 600 h on stream test, showing potential for practical implementation.

Aiming to mitigate anthropogenic CO₂ and utilize it as a valuable product, CO₂ hydrogenation to methanol has received extensive interest from academia and industry^{1–5}. Carbon Recycling International established the world's first large-scale CO₂-to-methanol plant using Cu/ZnO/Al₂O₃, a classical catalyst originally developed and optimized for syngas-to-methanol conversion⁶. Numerous efforts are still being undertaken to elucidate the active site and optimize catalyst activity^{7–10}. Nevertheless, one of the critical limitations of Cu/ZnO/Al₂O₃ is deactivation due to the unsatisfactory stability of the catalyst under exposure to heat and moisture, hampering long-term process operation^{11–14}. Consequently, several Cu-free metal oxides have been reported as new classes of catalysts for CO₂ hydrogenation to methanol^{15–19}, among which, ZnO-ZrO₂ solid solution catalyst (ZnZrO_x) reported by Li and co-workers¹⁸ is undergoing pilot-scale testing²⁰. One distinctive feature of ZnZrO_x is its superior long-term stability;

however, a downside is its lower activity compared to Cu/ZnO/Al₂O₃. Achieving both high activity and long-term stability is a challenging mission for developing next-generation CO₂ hydrogenation catalysts.

Since H₂ activation over metal oxide catalysts is often kinetically limited^{16,21,22}, the metal promotion has been widely explored for improving methanol formation activity. In particular, for ZnZrO_x, various metals such as Cu²³, Pt²³, Ga²⁴, and Pd^{22,23,25} have been reported as effective metal promoters. It is a general belief that the metal promoter and oxide support should be placed close to each other to maximize interfacial synergy (including strong metal-support interaction), and thus, various synthetic techniques were developed to anchor metal promoters directly on the oxide catalyst surface^{26–38}. Previously, we studied Pd-promoted ZnZrO_x catalyst (Pd/ZnZrO_x) for methanol formation²², revealing that the major role of Pd is to activate and split H₂ into H atoms that are subsequently transferred to adjacent Zn sites

¹Department of Chemical and Biomolecular Engineering, National University of Singapore, 4 Engineering Drive 4, Singapore 117585, Singapore. ²Department of Chemical and Biomolecular Engineering, KAIST, Daejeon 34141, Republic of Korea. ³Institute of Sustainability for Chemical, Energy and Environment, Agency for Science, Technology and Research (A*STAR), Singapore 627833, Singapore. ⁴Department of Chemistry, National Tsing Hua University, Hsinchu 300044, Taiwan. ⁵Frontier Research Center on Fundamental and Applied Sciences of Matters, National Tsing Hua University, Hsinchu 300044, Taiwan.

✉ e-mail: cheserg@nus.edu.sg; ning.yan@nus.edu.sg

for methanol synthesis. Thus, the rate of H supply to the active sites was identified as a key factor governing the rate of CO₂ reduction to methanol. However, at present, there are limited ways to enhance the interfacial area between the Pd promoter and ZnZrO_x catalyst for traditional metal/oxide nanocomposite catalysts.

Herein, we address this challenge by combining ZnZrO_x with Pd supported on carbon nanotubes (CNT): Pd/CNT + ZnZrO_x. CNT is a well-known material for hydrogen storage^{39–41}, and doping CNT with metal- or metal oxide- greatly enhances its H storage capacity, hinting at swift hydrogen transfer between CNT and the dopants^{40–44}. Moreover, Crossley and co-workers conducted an elegant study of the nature of active sites on Pd/TiO₂ and Cu/TiO₂ catalysts in furfural and anisole hydrogenations by separating metal from the support by a controlled distance using CNT, further substantiating that CNT may act as a bridge between metal and oxide⁴⁵. Torrente-Murciano and co-workers reported the superiority of graphitized CNT as a support for Ru catalysts in NH₃ cracking, due to the electronic modification of Ru particles by CNT⁴⁶. Based on these previous reports, and the unique property of CNT, we presumed that Pd/CNT can deliver hydrogen to ZnZrO_x via hydrogen activation on Pd and spillover via CNT. Our experiments showed that Pd/CNT + ZnZrO_x features drastically improved methanol formation activity from CO₂ compared to not only ZnZrO_x, but also Pd/ZnZrO_x with the same Pd content. The Pd/CNT + ZnZrO_x additionally exhibits excellent long-term stability, surpassing the performance of the state-of-the-art Cu/ZnO/Al₂O₃ industrial catalysts during the on-stream test from 200 h onwards.

Results

Preparation and characterization of the catalysts

The structures of ZnZrO_x, Pd/ZnZrO_x, and Pd/CNT + ZnZrO_x catalysts were characterized using various techniques. According to TEM and SEM analyses, ZnZrO_x is composed of ca. 10–15 nm crystallites, which are present as agglomerated ~μm-scale particles (Supplementary Fig. 1). Pd/CNT contains uniformly dispersed Pd nanoparticles (ca. 5 nm) inside and outside the carbon tubes. (Supplementary Fig. 2). XRD analysis proves that ZnZrO_x has a *t*-ZrO₂ phase-like crystalline

solid solution structure⁴⁸. The crystallinity of ZnZrO_x is well-preserved after Pd-impregnation as well as physical mixing with Pd/CNT (Fig. 1a). The TEM image of Pd/ZnZrO_x shows the presence of ca. 5 nm Pd nanoparticles on the surface of ZnZrO_x (Fig. 1b). In Pd/CNT + ZnZrO_x, the majority of Pd particles are present far away from the ZnZrO_x surface (Fig. 1c). As Pd/CNT and ZnZrO_x entangle with each other (Fig. 1c, d), EDX elemental mapping in the 2D-projection shows a uniform distribution of Pd over the catalyst domain (Fig. 1e). H₂- and CO-chemisorption analysis confirms that Pd/ZnZrO_x and Pd/CNT have a similar Pd dispersion of 18–20%, which is consistent with TEM analysis. Of note, Pd dispersion is not altered during physical mixing (Supplementary Table 1). Based on these results, we present an illustration of the three catalysts in Fig. 1f. Furthermore, Pd/GNP (GNP: graphene nanoplatelets), Pd/AC (AC: activated carbon), Pd/SiO₂ and Pd/TiO₂ were prepared and mixed with ZnZrO_x as control samples. The characterizations of these catalysts are included in Supplementary Figs. 3, 4 and Supplementary Table 1. The general observations about their structural features are very similar to those of Pd/CNT and Pd/CNT + ZnZrO_x.

Unique CO₂ hydrogenation performance of Pd/CNT + ZnZrO_x

The activities of ZnZrO_x and various Pd-promoted ZnZrO_x catalysts for CO₂ hydrogenation to methanol (MeOH) were investigated under the reaction kinetics-controlled region (conditions: 533 K, 5 MPa total pressure with CO₂/H₂/Ar = 19/76/5 (molar), conversion: 0.64–1.36%). The exclusion of external and internal mass transfer limitation is described in Section 3 in Supplementary Information.

CO₂ conversion and product selectivity of the catalysts are shown in Supplementary Table 2. For all catalysts, the major products are methanol and CO. Only Pd/SiO₂ + ZnZrO_x and Pd/TiO₂ + ZnZrO_x produced CH₄ (≤3.40%) and dimethyl ether (DME, ≤0.14%) as side products. Since standalone Pd catalysts have negligible methanol formation activity compared to ZnZrO_x (Supplementary Fig. 5), the methanol formation rate (*r*_{MeOH}) of ZnZrO_x-containing catalysts in Fig. 2a was represented based on the mass of ZnZrO_x. Pd/ZnZrO_x exhibits higher *r*_{MeOH} (3.96 mmol g_{ZnZrO_x}⁻¹ h⁻¹) than ZnZrO_x (1.69 mmol g_{ZnZrO_x}⁻¹ h⁻¹), illustrating the promotional effect from surface Pd

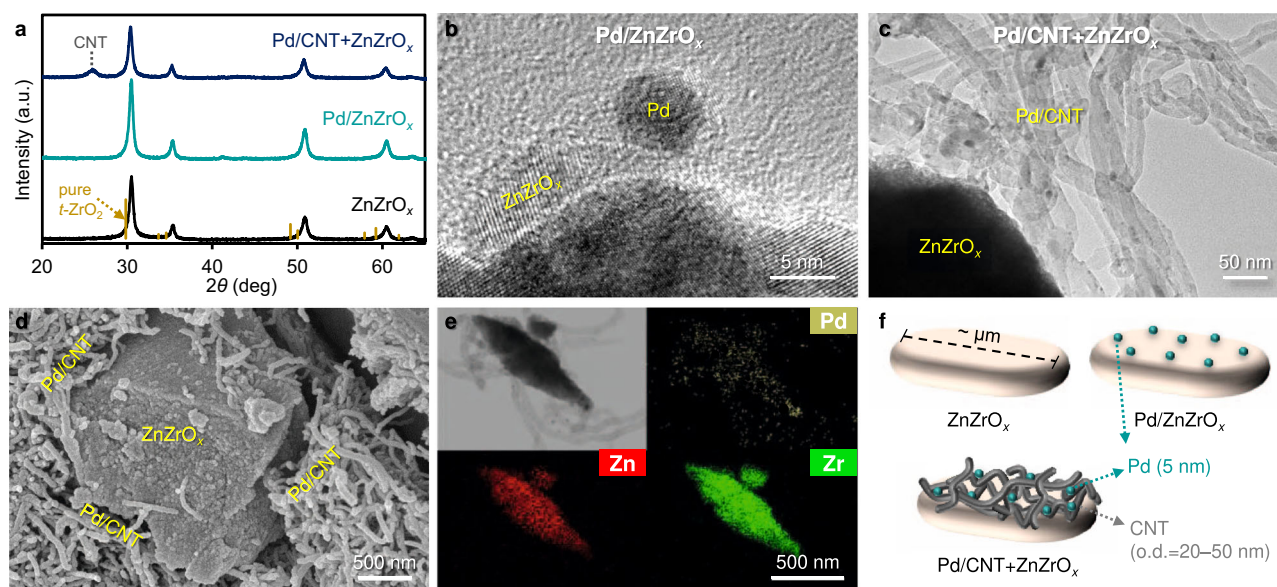


Fig. 1 | Structural characterization of catalysts. **a** Powder XRD patterns of ZnZrO_x, Pd/ZnZrO_x, and Pd/CNT + ZnZrO_x. The peak shift to higher 2θ of ZnZrO_x compared to pure ZrO₂ indicates the substitution of Zr atoms to Zn atoms (i.e., solid solution formation). The XRD pattern of pure *t*-ZrO₂ is obtained from Materials Data

on ZrO₂ by Materials Project, ID: mp-2574. **b** TEM image of Pd/ZnZrO_x. **c** TEM image of Pd/CNT + ZnZrO_x. **d** SEM image of Pd/CNT + ZnZrO_x. **e** EDX elemental maps of Pd/CNT + ZnZrO_x during TEM analysis. **f** Illustration of the structures for ZnZrO_x, Pd/ZnZrO_x, and Pd/CNT + ZnZrO_x catalysts (o.d. outer diameter).

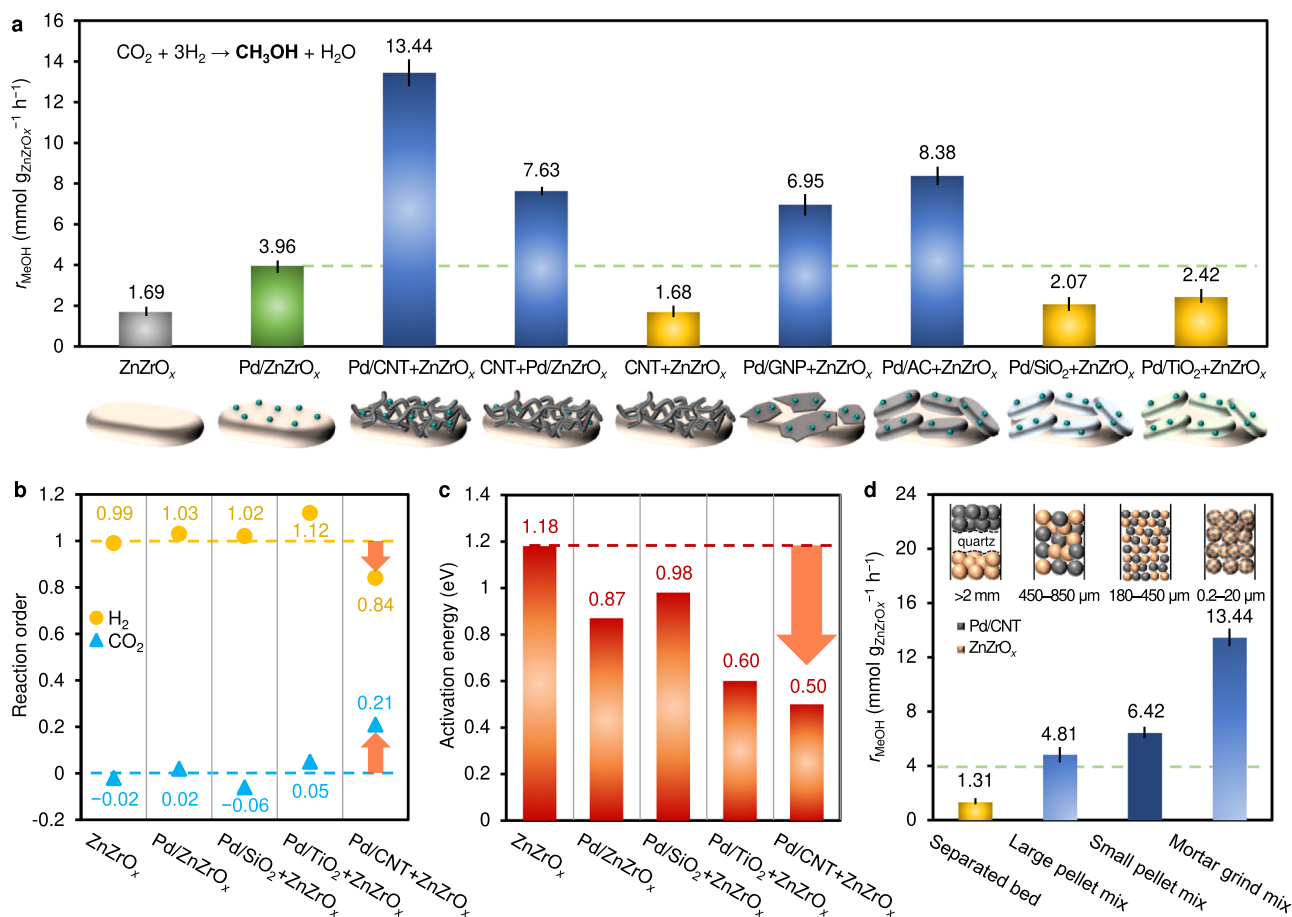


Fig. 2 | Analysis of reaction kinetics of ZnZrO_x and Pd-promoted ZnZrO_x catalysts in the CO₂ hydrogenation to methanol. **a** Methanol formation rate (r_{MeOH}) over ZnZrO_x-based catalysts (Condition: 533 K, 5 MPa, CO₂/H₂/Ar = 19/76/5 (molar), gas hourly space velocities (GHSV) are shown in Supplementary Table 2). **b** Reaction orders with respect to H₂ and CO₂ for methanol formation. **c** Apparent

activation energy for methanol formation. The values were determined by the Arrhenius plot shown in Supplementary Fig. 7. **d** Effect of catalyst mixing configurations on methanol formation in the combination of Pd/CNT and ZnZrO_x. Inset shows the illustration of each mixing configuration. The green dashed line in Fig. **a**, **d** indicates the activity of Pd/ZnZrO_x.

nanoparticles. Unexpectedly, a higher r_{MeOH} is observed over Pd/CNT + ZnZrO_x (13.44 mmol g_{ZnZrO_x}⁻¹ h⁻¹) compared to Pd/ZnZrO_x, which is an exceptional finding, since the metal promoter (Pd) induces a significantly more pronounced effect when away from the active sites on ZnZrO_x. Considering that Pd/ZnZrO_x and Pd/CNT + ZnZrO_x possess similar Pd dispersion and identical Pd loading with respect to ZnZrO_x (Supplementary Table 1), and that no promotion was observed when ZnZrO_x is mixed with CNT (CNT + ZnZrO_x), both Pd and CNT are concluded to be essential for the superior catalytic performance of Pd/CNT + ZnZrO_x. A strong promoting effect is also observed when Pd/ZnZrO_x is mixed with CNT (i.e., r_{MeOH} = 7.63 mmol g_{ZnZrO_x}⁻¹ h⁻¹ for CNT + Pd/ZnZrO_x) as well as when ZnZrO_x is mixed with other carbon-supported Pd catalysts (i.e., Pd/GNP + ZnZrO_x, Pd/AC + ZnZrO_x). In contrast, when ZnZrO_x is mixed with Pd/oxide catalysts such as Pd/SiO₂ and Pd/TiO₂ (i.e., Pd/SiO₂ + ZnZrO_x, Pd/TiO₂ + ZnZrO_x), there is only slight promotion, demonstrating the unique role of carbon supports. Although TiO₂ is a well-known reducible oxide for fast hydrogen spillover, Pd/TiO₂ has an order of magnitude higher CO₂ hydrogenation activity toward CO compared to other Pd/support catalysts (Supplementary Fig. 5). Thus, Pd/TiO₂ converts CO₂ and H₂ by itself rather than acting as a ‘hydrogen dispenser’. These observations indicate promoting performance is related to hydrogen spillover efficiency, which strongly depends on the type of support as hydrogen moves as an H⁺/e⁻ pair^{47–49}.

In reaction kinetic analyses (Fig. 2b and Supplementary Fig. 6), the reaction orders with respect to H₂ (n_{H_2}) and CO₂ (n_{CO_2}) for methanol

synthesis over ZnZrO_x are ca. 1.0 and 0, respectively. The results imply that the surface coverage of H₂ is much lower than that of CO₂. The n_{H_2} = ca. 1.0 suggests that H₂ activation may be a rate-determining step. Pd/ZnZrO_x catalyst shows similar n_{H_2} and n_{CO_2} values to those of pristine ZnZrO_x. In contrast, there is a substantial decrease of n_{H_2} (0.84) alongside a simultaneous increase of n_{CO_2} (0.21) for Pd/CNT + ZnZrO_x. The result indicates the coverage of hydrogen on the ZnZrO_x surface increased considerably through combination with Pd/CNT. As shown in Fig. 2c and Supplementary Fig. 7, Pd/CNT + ZnZrO_x exhibits drastically decreased apparent activation energy (E_a = 0.50 eV) compared to ZnZrO_x (E_a = 1.18 eV), confirming the immense contribution of physical mixing with Pd/CNT on accelerating reaction kinetics.

For the ZnZrO_x and Pd/CNT combination, the effect of mixing configuration was studied to gain insight into the origin of promotion (Fig. 2d). Four different mixing configurations were prepared by varying the mixing method, namely separated bed, large pellet mix (size: 450–850 μm), small pellet mix (size: 180–450 μm), and mortar grind mix (size: 0.2–20 μm). The separated bed configuration gives a detrimental effect on methanol formation, implying the promoting effect in Pd/CNT + ZnZrO_x is not originated from the transport of intermediates in the gas-phase. On the other hand, a higher activity compared to pristine ZnZrO_x was detected for all other configurations. The promoting effect is strengthened as the contact between the two components (Pd/CNT and ZnZrO_x) increases, reaching the maximum in the mortar grind mix configuration. It is noteworthy that even when

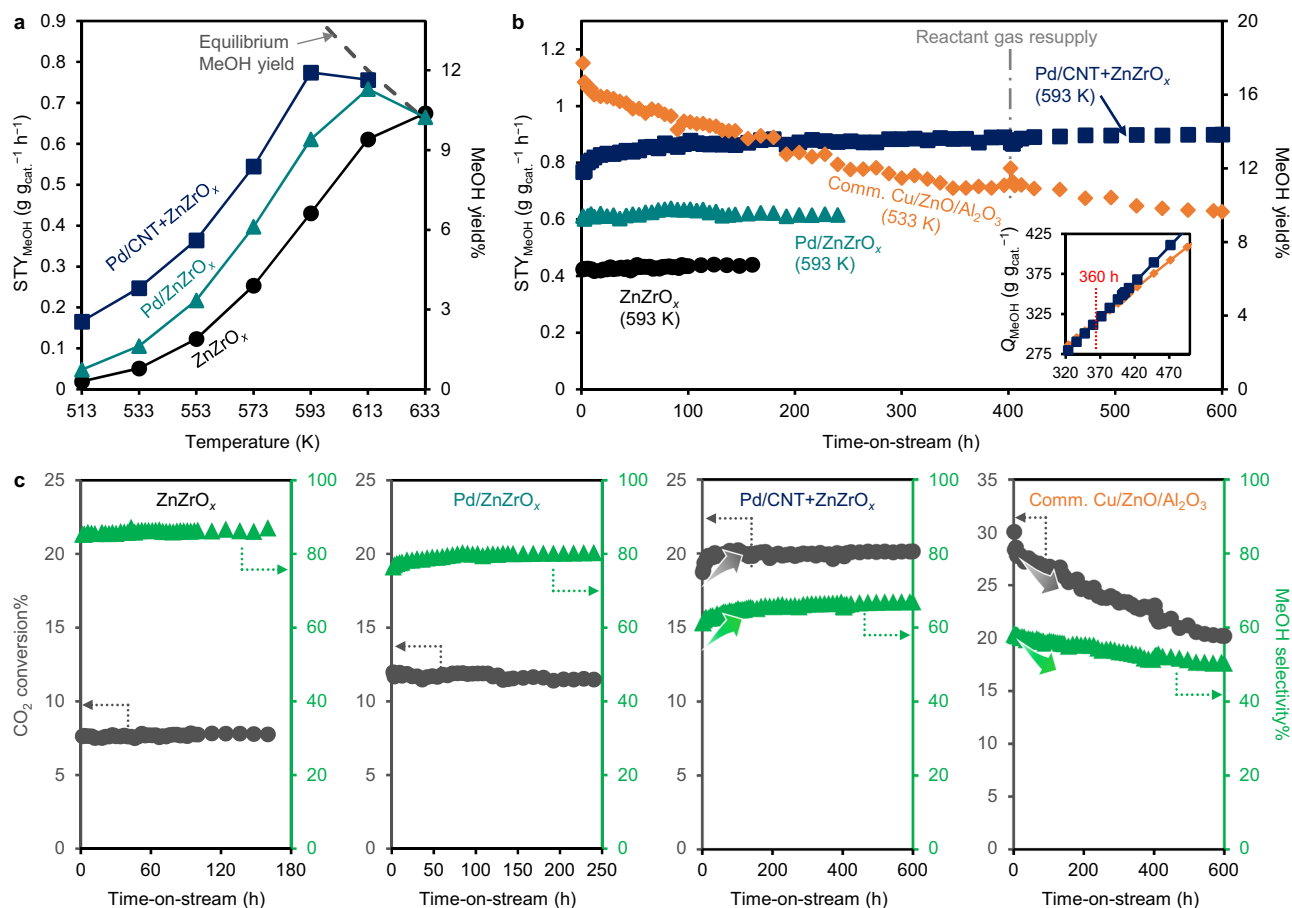


Fig. 3 | Catalytic performance of Pd/CNT + ZnZrO_x in industry-relevant conditions. **a** Methanol yield and STY_{MeOH} of the ZnZrO_x-based catalysts as a function of reaction temperature. The dashed line indicates the methanol yield at thermodynamic equilibrium. **b** Long-term catalytic tests of ZnZrO_x-based catalysts (593 K), and commercial Cu/ZnO/Al₂O₃ (533 K). The inset shows cumulative

methanol production (Q_{MeOH} , g g_{cat.}⁻¹) as a function of time-on-stream (Condition: 5 MPa, CO₂/H₂/Ar = 19/76/5, GHSV = 24,000 cm³_{STP} g_{cat.}⁻¹ h⁻¹). **c** CO₂ conversion and methanol selectivity changes during long-term reaction test over ZnZrO_x, Pd/ZnZrO_x, Pd/CNT + ZnZrO_x, and commercial Cu/ZnO/Al₂O₃ catalysts.

the two components are mixed in 180–850 μm-scale, the promoting effect ($r_{\text{MeOH}} = 4.81\text{--}6.42 \text{ mmol g}_{\text{ZnZrO}_x}^{-1} \text{ h}^{-1}$) is stronger than that of Pd/ZnZrO_x (Fig. 2a, $r_{\text{MeOH}} = 3.96 \text{ mmol g}_{\text{ZnZrO}_x}^{-1} \text{ h}^{-1}$). This result firmly demonstrates the effectiveness of the strategy for hydrogen delivery; hydrogen transfer efficiency is no longer limited by the number of Pd-ZnZrO_x interface sites, but rather by the closeness of ZnZrO_x particles and CNT.

We further tested the performance of Pd/CNT + ZnZrO_x under industry-relevant reaction conditions (5 MPa, GHSV = 24,000 cm³_{STP} g_{cat.}⁻¹ h⁻¹) to evaluate the practical potential of this catalyst. First, CO₂ conversion and selectivity of products at different temperatures (513–633 K) are summarized in Supplementary Table 3. The result indicates that methanol and CO are the major products under these reaction conditions. The selectivity of Pd/CNT + ZnZrO_x is lower than that of ZnZrO_x and Pd/ZnZrO_x due to the CO formation activity of Pd/CNT itself (Supplementary Fig. 5). Nevertheless, the MeOH selectivity gap between Pd/CNT + ZnZrO_x and ZnZrO_x is less than 10% at the same CO₂ conversion level (Supplementary Fig. 8).

Methanol yield and corresponding space-time yield of methanol (STY_{MeOH}) were monitored while varying reaction temperature (Fig. 3a). The STY_{MeOH} for Pd/CNT + ZnZrO_x is 0.780 g g_{cat.}⁻¹ h⁻¹ at 593 K, the highest value among all reported ZnZrO_x-based catalysts (Supplementary Table 4). Moreover, the long-term stability of each catalyst was monitored at 593 K while a commercial Cu/ZnO/Al₂O₃ catalyst was simultaneously introduced as a control sample. As shown in Supplementary Fig. 9, the optimal reaction temperature for

Cu/ZnO/Al₂O₃ catalyst that shows the maximum STY_{MeOH} is 533 K (thermodynamic equilibrium MeOH yield = 24%), thus the long-term test was conducted at this temperature for Cu/ZnO/Al₂O₃. Not unexpectedly, Cu/ZnO/Al₂O₃ exhibits relatively high activity initially but shows rapid deactivation from the beginning (Fig. 3b); after 600 h of reaction, 46% of initial activity has been lost. In contrast, Pd/CNT + ZnZrO_x catalyst shows superior long-term performance; the methanol yield over Pd/CNT + ZnZrO_x reaches 13.5% (STY_{MeOH} = 0.90 g g_{cat.}⁻¹ h⁻¹) at 600 h time-on-stream, very close to the value at thermodynamic equilibrium (MeOH yield = 14.0% at 593 K). XANES and EXAFS analyses after the reaction reveal that there are no substantial changes in the chemical state of either Zn or Zr in Pd/CNT + ZnZrO_x, validating the superior stability of Pd/CNT + ZnZrO_x (Supplementary Figs. 10–11). Both catalysts were additionally tested at a higher GHSV (80,000 cm³_{STP} g_{cat.}⁻¹ h⁻¹) to shift conversion further away from thermodynamic equilibrium. Again, Cu/ZnO/Al₂O₃ exhibited continued deactivation while the Pd/CNT + ZnZrO_x system kept increasing its methanol productivity during a 104 h test. (Supplementary Fig. 12). Compared to ZnZrO_x and Pd/ZnZrO_x, distinct increases in conversion and methanol selectivity are observed for Pd/CNT + ZnZrO_x, particularly during the initial stage of reaction (Fig. 3c). Under the steady state (time-on-stream >400 h), Pd/CNT + ZnZrO_x shows 66% methanol selectivity at 20% CO₂ conversion, higher than the methanol selectivity of Cu/ZnO/Al₂O₃ at comparable CO₂ conversion (50–52% at 23–20% CO₂ conversion). As a result of the opposite activity variation trend, cumulative methanol production (Q_{MeOH}) of

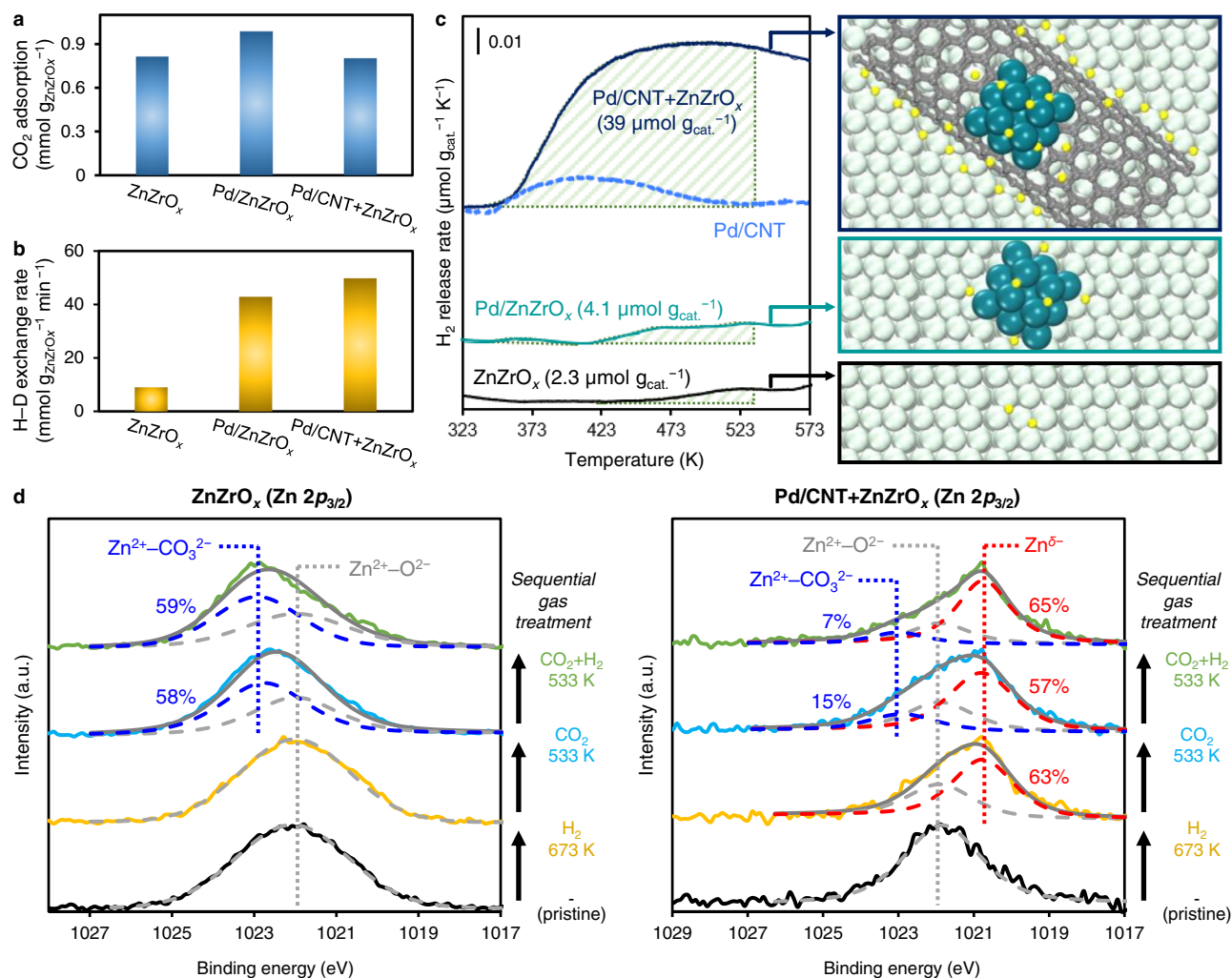


Fig. 4 | Quantitative gas adsorption-desorption analysis of catalysts. **a** CO₂ adsorption capacity of catalysts determined by CO₂-TPD. **b** H-D exchange rate of catalysts at 373 K. **c** H₂-TPD profile and quantification of reversible H₂ of catalysts. The quantification of reversible H₂ was conducted by integrating the peak area in

the range of 323–533 K which is below the temperature of our reaction kinetic analysis. **d** Zn 2p_{3/2} XPS of ZnZrO_x and Pd/CNT + ZnZrO_x catalysts before and after sequential gas treatments (gas treatment condition: H₂ at 673 K, CO₂ at 533 K, and CO₂ + H₂ (1:4) at 533 K).

Pd/CNT + ZnZrO_x overwhelms that of commercial Cu/ZnO/Al₂O₃ after 360 h reaction (Fig. 3b, inset). At 600 h, Pd/CNT + ZnZrO_x offered a 1.44-fold higher methanol yield over the commercial Cu/ZnO/Al₂O₃ catalyst, and its STY_{MeOH} (g g_{cat.}⁻¹ h⁻¹) compare favorably with state-of-the-art catalysts, that were scrutinized in long-term stability tests in the literature (Supplementary Table 5), further validating the superior performance of the Pd/CNT + ZnZrO_x catalyst. In addition, Pd/CNT + ZnZrO_x contains 33 wt% CNT, which can act as a catalyst binder/diluent due to its high mechanical strength⁵⁰ and thermal conductivity⁵¹. Therefore, Pd/CNT + ZnZrO_x may not require further use of an extra binder/diluent, providing additional benefits for practical implementation.

Characterization of the promotion effect in Pd/CNT + ZnZrO_x

The origin of promotion was elucidated by quantitative gas adsorption-desorption analyses. CO₂-TPD profiles reveal ZnZrO_x, Pd/ZnZrO_x, and Pd/CNT + ZnZrO_x have comparable adsorption strengths (Supplementary Fig. 13) and capacity of CO₂ (Fig. 4a), indicating CO₂ adsorption properties of the catalysts are similar. H₂-D₂ isotope exchange experiments were then conducted at 373 K (Fig. 4b) to determine their H₂ activation function. ZnZrO_x shows a low H-D exchange rate (8.93 mmol g_{ZnZrOx}⁻¹ min⁻¹), while Pd/ZnZrO_x and Pd/CNT + ZnZrO_x show accelerated rates at 42.9 and

49.8 mmol g_{ZnZrOx}⁻¹ min⁻¹, respectively. We draw two major conclusions from these isotope exchange experiments. First, Pd species easily activate H₂, regardless of whether Pd nanoparticles are directly supported on ZnZrO_x or on CNT. Second, the H₂ activation function alone is not the critical factor in determining methanol formation activity, since the H-D exchange rates on Pd/ZnZrO_x and Pd/CNT + ZnZrO_x are comparable despite their pronounced difference in methanol production.

Next, H₂-TPD profiles of various catalysts were examined to differentiate their ability in delivering activated hydrogen (H*) (Fig. 4c). ZnZrO_x shows an H₂ desorption peak above 423 K, while Pd-containing catalysts exhibit a peak starting from 343 K due to more facile desorption of H₂ from the Pd surface. The amounts of adsorbed H₂ on ZnZrO_x and Pd/ZnZrO_x were 2.3 and 4.1 μmol g_{cat.}⁻¹, respectively. In sharp contrast, Pd/CNT + ZnZrO_x shows an order of magnitude increase in H₂ adsorption (39 μmol g_{cat.}⁻¹). Considering Pd/CNT alone only possesses 7.1 μmol H₂ g_{cat.}⁻¹, and that Pd/CNT accounts for one-third of the mass in the mixture catalyst, over 90% of the adsorbed hydrogen in the Pd/CNT + ZnZrO_x mixture is stored at the interfaces between ZnZrO_x and CNT, which undergo reverse spillover during TPD analysis (Fig. 4c, right panels). In the case of Pd/SiO₂ and Pd/TiO₂, there are only marginal increments in the H₂ adsorption capacity after physical mixing with ZnZrO_x (Supplementary Fig. 14), confirming the unique property of CNT as a hydrogen delivery system. Band gap

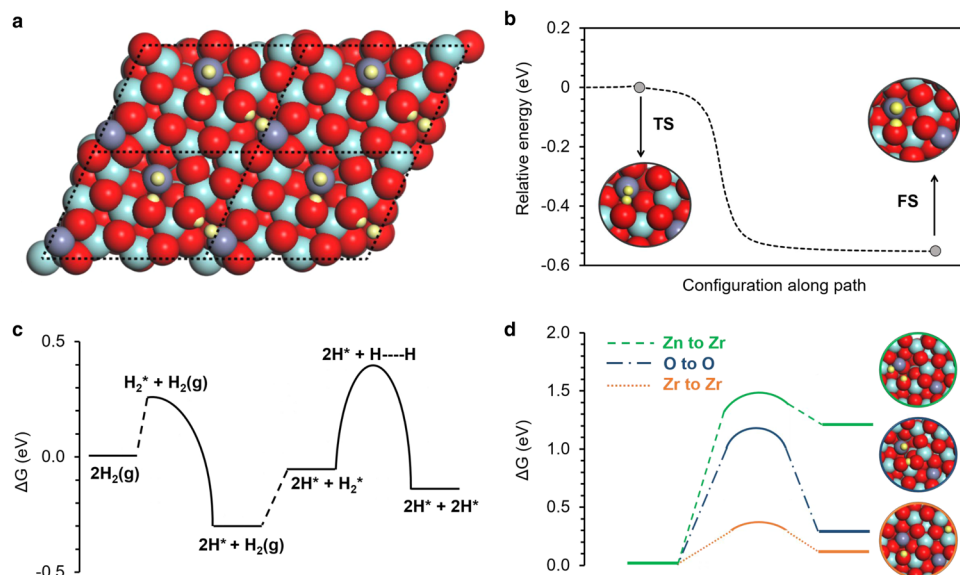


Fig. 5 | Simulations of H atoms on the bare ZnZrO_x surface. **a** Top view of four employed ZnZrO_x supercells illustrating 4 H atoms adsorbed per unit cell on Zn–O pairs, formed after successive dissociation of two H₂ molecules. **b** Potential energy profile along the reaction coordinate for barrierless dissociation of the first H₂ molecule (TS transition state, FS final state). **c** Potential energy profile of successive

H₂ dissociation at ZnZrO_x for 2 H₂ molecules. **d** Energy profile for H movement from Zn to Zr, O to O, and Zr to Zr on the ZnZrO_x surface. The inset images show the transition state configurations. Turquoise, purple, red, and yellow colors represent Zr, Zn, O, and H, respectively.

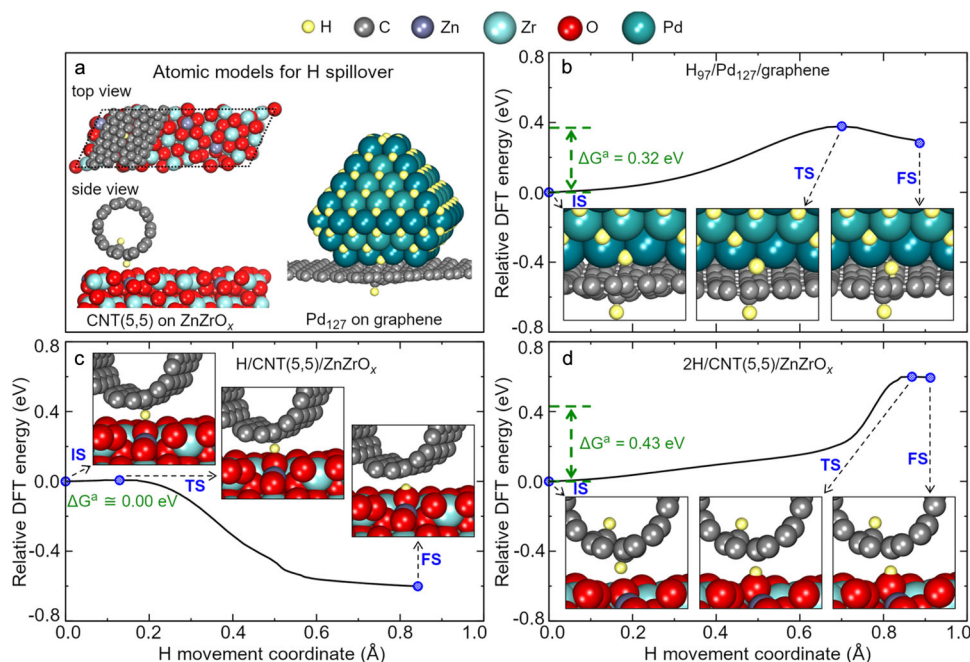


Fig. 6 | Simulations of hydrogen spillover in Pd/CNT + ZnZrO_x. **a** Atomic models of CNT(5,5) on ZnZrO_x and Pd on carbon (a graphene sheet) for H spillover. **b** Energy profile for movement of one H from hydrogen-saturated Pd to the graphene sheet with a pre-adsorbed H atom (IS initial state, TS transition state, and FS

final state). **c** Energy profile for spillover of the single H atom from CNT(5,5) to ZnZrO_x. **d** Energy profile for spillover of one H atom from CNT(5,5) with another H atom adsorbed on it to ZnZrO_x.

analysis suggests carbonaceous materials have much smaller band gap values (0.74–0.75 eV) compared to metal oxides (≥ 3.09 eV) including ZnZrO_x (Supplementary Fig. 15), suggesting higher electrical conductivity results in faster migration kinetics of hydrogen (H⁺/electron pair) on the carbon surface versus oxides such as ZnZrO_x.

X-ray photoelectron spectroscopy (XPS) after sequential gas treatments (without sample exposure to air) for ZnZrO_x and Pd/CNT + ZnZrO_x were carried out to provide more insight into the

hydrogen spillover. The spectra of each element are demonstrated in Supplementary Figs. 16–20, while the XPS of Zn 2p_{3/2} region is represented in Fig. 4d. Before gas treatment, ZnZrO_x and Pd/CNT + ZnZrO_x show identical symmetric Zn 2p_{3/2} signals at 1022 eV which represent Zn²⁺ bound to lattice oxygen (Zn²⁺–O²⁻). After H₂ treatment at 673 K, ZnZrO_x shows no signal changes, whereas Pd/CNT + ZnZrO_x exhibits the formation of a shoulder peak at -1 eV lower binding energy region. The transformation of Zn²⁺–O²⁻ to reduced Zn species (Zn^δ)^{52,53} is a

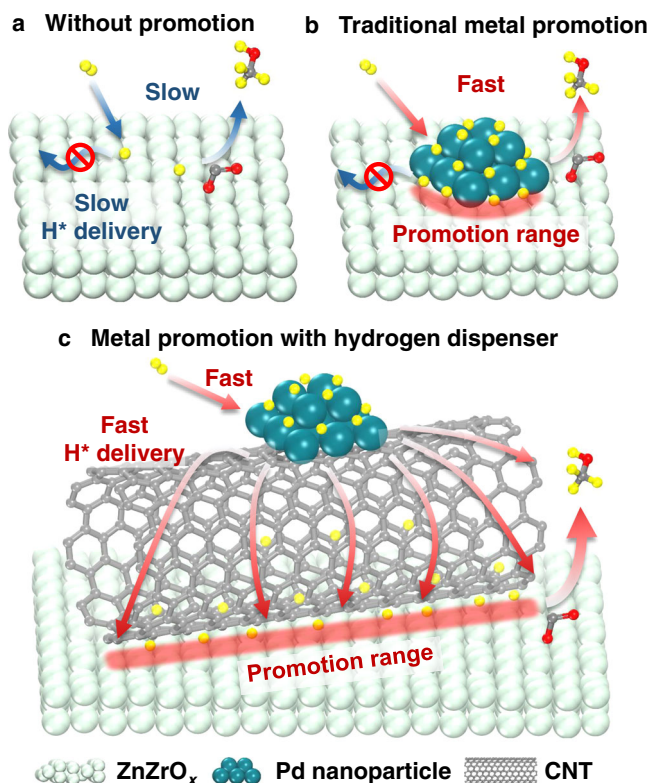


Fig. 7 | Schematic illustration of the effect of catalyst structure on CO_2 hydrogenation to methanol. **a** ZnZrO_x catalyst without any metal promotion. **b** Pd-supported ZnZrO_x catalyst which represents the traditional metal/oxide catalyst harnessing metal promotion. **c** Pd/CNT + ZnZrO_x catalyst which represents a conceptually new catalyst system harnessing metal promotion with a hydrogen dispenser.

result of electron transfer from spilt over hydrogen to the Zn site of the ZnZrO_x surface. Both H_2 -reduced catalysts were further treated with CO_2 and $\text{CO}_2 + \text{H}_2$ after which a shoulder peak at -1 eV higher binding energy region appears, indicative of CO_2 chemisorption on Zn-O pair ($\text{Zn}^{2+}-\text{CO}_3^{2-}$)⁵³. Notably, the existence of Zn^{δ} species is still pronounced in Pd/CNT + ZnZrO_x after consecutive treatments with CO_2 and $\text{CO}_2 + \text{H}_2$. The portion of Zn^{δ} is slightly decreased after CO_2 treatment (from 63 to 57%), but it recovers the original fraction when treated with $\text{CO}_2 + \text{H}_2$ (65%), providing evidence of effective hydrogen spillover in the Pd/CNT + ZnZrO_x system under CO_2 hydrogenation condition.

Computational studies on hydrogen spillover in Pd/CNT + ZnZrO_x

Density functional theory calculations were applied to provide an atomistic description of hydrogen spillover in the Pd/CNT + ZnZrO_x nanocomposite. After identifying the most stable model for ZnZrO_x (Supplementary Figs. 21–24), we studied the adsorption and movement of H on the bare ZnZrO_x surface (Fig. 5 and Supplementary Fig. 25). H_2 dissociation on pure ZrO_2 is kinetically limited⁵⁴, which can be improved by doping the oxide with Zn atoms^{18,55}. We calculated Zn-O pairs in the ZnZrO_x surface to have the lowest dissociative adsorption energies of H_2 among all surface sites (Supplementary Fig. 25b). Since our ZnZrO_x supercell contains two Zn sites (Fig. 5a), we are able to perform simulations for the sequential dissociation of two H_2 molecules. The dissociation of the first H_2 molecule is a barrierless step (Fig. 5b) with reaction energy of $\Delta G = -0.31$ eV (Fig. 5c). Yet, the dissociation of the second H_2 molecule is impaired by a higher activation barrier ($\Delta G^\ddagger = 0.71$ eV) and reaction energy of $\Delta G = 0.17$ eV (Fig. 5c), indicating limited H coverage on unmodified ZnZrO_x under reaction conditions.

Moreover, H atoms are calculated to have negligible mobility on the ZnZrO_x surface with barriers up to $\Delta G^\ddagger = 1.18$ eV for diffusion between O sites and $\Delta G^\ddagger = 1.51$ eV for migration of H atoms from Zn to Zr atoms (Fig. 5d). Although a much lower barrier of $\Delta G^\ddagger = 0.34$ eV was calculated for H diffusion between Zr sites, these sites were calculated to be up to 2.22 eV less stable for H than O sites on ZnZrO_x surface based on the adsorption energy of one H atom. These suggest that directly supported Pd nanoparticles cannot deliver reactive H atoms to the active sites on ZnZrO_x since long-distance H spillover is hindered by high diffusion barriers of H atoms on the oxide surface.

In contrast to the bare ZnZrO_x , our calculations show that H can be fluently supplied to the active sites on the ZnZrO_x surface via spillover from Pd/CNT (Fig. 6). We created models of physisorbed CNT on ZnZrO_x using an adapted lattice matching algorithm, which ensured the minimal strain of -2.33% along the CNT length (Fig. 6a). According to our simulations, a single H atom bind stronger to ZnZrO_x than to CNT, which creates a significant thermodynamic driving force for the spillover and makes this process essentially barrierless (Fig. 6c). However, the spillover barrier increases when more H atoms are adsorbed on CNT. For example, the Gibbs barrier for the spillover of an H atom from CNT to ZnZrO_x increases to 0.43 eV when another H atom is adsorbed in the most stable position on the vicinal site on the inner side of the nanotube (Fig. 6d). In turn, H spillover from CNT to ZnZrO_x becomes endothermic by about $\Delta G = 2.5$ eV when every C atom of CNT is hydrogenated. In conclusion, low H coverage on CNT can be regarded as the critical structural factor enabling hydrogen spillover from C to the oxide. Low H coverage on CNTs is also suggested by our XPS studies showing mostly sp^2 hybridization of C atoms in the CNT under reaction conditions (Supplementary Fig. 19).

To evaluate the rate of H spillover from Pd to sp^2 carbon, we simulated the movement of H from a 1.56 nm large Pd_{127} fcc nanocrystallite to a graphene sheet representing a broad nanotube. We chose the shape of the Pd_{127} particle in line with TEM data and identified the most stable structure of the Pd_{127} /graphene interface by screening all high-symmetry interfaces (Supplementary Fig. 26). Our calculations show that the barriers for H spillover from Pd to graphene are essentially governed by the endothermicity of this process (Fig. 6b), which depends on the H coverage. Namely, the spillover of the first H atom from Pd_{127} to graphene is endothermic by $\Delta G = 1.57$ eV, which decreases to $\Delta G = 0.37$ eV when another H atom is present on the graphene sheet. Since the Gibbs adsorption energy per H atom of one (two) H on the freestanding CNT(5,5) is 1.04 eV (0.70 eV/H atom), which is 0.84 eV (0.37 eV/H atom) stronger than on graphene, the curvature of the CNT should further favor the transfer of H from Pd to the carbon domain. Thus, the barriers for H spillover from Pd to CNT are estimated to be much lower than the activation energy of H_2 dissociation on ZnZrO_x ($\Delta G^\ddagger = 0.71$ eV). In turn, CNTs are well known to be excellent transport channels for H atoms⁴⁵, whose movement over graphene was shown to be enabled by quantum tunneling⁵⁶. Thus, our simulations suggest a much faster H supply to the active sites on Pd/CNT + ZnZrO_x nanocomposite compared to the pristine ZnZrO_x .

Effect of catalyst structure on catalytic results in CO_2 -to-methanol

A number of studies using metal/support catalysts (e.g., Cu or Pd on ZnO, ZrO_2 , or ZnZrO_x) refer to hydrogen spillover as an important process for methanol synthesis from CO/CO_2 ^{23,57–63}, but it is difficult to disentangle catalytic activity generated by sites adjacent to metals from that generated by sites farther away⁶⁴. In Fig. 7, we present the effect of the catalyst structure on CO_2 hydrogenation to methanol over Pd-promoted ZnZrO_x catalysts. ZnZrO_x is an excellent material to chemisorb CO_2 , but methanol formation is limited due to low H_2 activation and H^* delivery capability (Fig. 7a). In turn, Pd particles supported on ZnZrO_x significantly enhance H_2 activation, but the delivery of H^* toward the active sites is hampered due to slow

H-migration kinetics within ZnZrO_x surface (Fig. 7b). It is estimated the contact area between Pd particles and ZnZrO_x is about 0.5 m² g_{cat.}⁻¹, only 1% of the entire catalyst surface area (estimation procedure available in Section 4 in Supplementary Information). Our experimental and computational studies support Prins's rigorous critique that hydrogen may not travel farther than the immediate interface between metal and basic oxide support⁴⁷, and Li et al.'s hypothesis that the rate-determining step of CO₂ hydrogenation to methanol over various catalysts (i.e., ZnZrO_x, Cu/ZnO/Al₂O₃, and Pd/ZnO) is the migration of H* on the catalyst surface⁶⁵. In the case of Pd/CNT + ZnZrO_x, CNT acts as a hydrogen dispenser, effectively delivering activated H* from Pd particles to the ZnZrO_x surface (Fig. 7c). Since the promotion range is determined by the contact area between CNT and ZnZrO_x, a ten-times larger promotion area is generated (as determined by H₂-TPD result) under mortar grind mode compared to traditional metal doping on the catalyst surface, leading to a drastically enhanced methanol formation rate. In the literature, non-contact integration of multiple catalytically active components, especially physical mixing, has been adopted in catalyst development for bifunctional- or cascade catalytic reactions for which each catalyst is responsible for one step of the entire transformation^{66–74}. Our work, in contrast, reports a bicomponent catalyst in which one component provides active sites for the formation of a target product while the other serves as an activation and delivery system for a kinetically hindered intermediate, which to our knowledge, has not been demonstrated for CO₂ hydrogenation.

Furthermore, our preliminary tests of physical mixing of commercial Cu/ZnO/Al₂O₃ with CNT results in 1.4 to 2.0-times higher methanol formation activity versus pristine Cu/ZnO/Al₂O₃ in the pressure range of 0.1–1.0 MPa (Supplementary Fig. 27), suggesting this promotion strategy is not limited to ZnZrO_x. For the successful implementation of the CO₂-to-MeOH process on large scales, recycling of the product stream (including unconverted CO₂, H₂, and produced CO) is necessary to intensify process economics^{75,76}. Future research should be directed to studying the effect of CO on nanoscale H supply in newly developed systems.

Discussion

Insufficient H₂ activation has long been known to limit the activity of oxide catalysts, such as ZnZrO_x, for CO₂ reduction to methanol. In this work, we report CNT as a hydrogen dispenser for enhancing hydrogen delivery to active sites on ZnZrO_x. The combination of Pd/CNT and ZnZrO_x leads to an exceptional catalytic system for methanol formation, far better than Pd/ZnZrO_x catalyst, as CNT effectively delivers Pd-activated hydrogen to a broad range of ZnZrO_x surface sites. The Pd/CNT + ZnZrO_x shows the highest STY_{MeOH} among reported non-Cu/ZnO-based catalysts to date and is durable over 600 h continuous operation, demonstrating its potential for practical implementation; concurrently, the physical mixing strategy offers a robust and transferable method for material integration to design better catalytic systems. This study provides an example in oxide catalyst design for which the transition metal promoter in non-contact mode induces a greater effect than the transition metal promoter directly attached to the surface of the catalytically active phase, expanding the concept of metal promotion beyond the traditional focus of metal-support interfaces.

Methods

Catalysts preparation

ZnO-ZrO₂ (Zn/Zr = 1/5) solid solution catalyst (ZnZrO_x) was prepared via a coprecipitation method with reference to the earlier literature²². An 1 wt% Pd/ZnZrO_x catalyst was prepared by wet impregnation using Pd(NO₃)₂·xH₂O as Pd precursor. To make the Pd/CNT + ZnZrO_x catalyst, 2 wt% Pd was first supported on CNT by wet impregnation followed by reduction at 673 K, and then Pd/CNT was physically mixed

with ZnZrO_x with Pd:ZnZrO_x = 1:100 mass ratio. Physical mixing was carried out by mortar grinding, unless otherwise stated. For comparison, various other physically mixed catalysts (Pd/support + ZnZrO_x) were also prepared in a similar manner while varying the support material (support = type of support used; AC: activated carbon, GNP: graphene nanoplatelet, SiO₂: silica, TiO₂: titania P25). CNT + ZnZrO_x and CNT + Pd/ZnZrO_x were also prepared by physical mixing of CNT and ZnZrO_x or Pd/ZnZrO_x. Prior to the characterizations and catalytic reactions, the catalysts were mortar ground. As shown in Section 5 in Supplementary Information, the mortar grinding itself does not significantly affect the surface area and catalytic activity of ZnZrO_x.

Catalyst characterization

The structures of catalysts were characterized using transmission electron microscopy (TEM) coupled with energy dispersive X-ray (EDX) elemental analysis, scanning electron microscopy (SEM), powder X-ray diffraction (XRD), N₂ physisorption, H₂ and CO chemisorption, CO₂- and H₂-temperature-programmed desorption (TPD), H₂-D₂ isotope exchange, UV-Vis-NIR spectroscopy, and X-ray photoelectron spectroscopy (XPS).

Catalytic test

CO₂ hydrogenation was carried out using an automatic multi-channel high-pressure flow reactor designed by PID Eng & Tech. Prior to the reaction, the catalysts were pressed, cracked, and sieved to make pellets. The sieved catalyst pellets (450–850 μm) were loaded into the reactor, and pretreated with H₂ (40 cm³_{STP} min⁻¹) at 673 K for 2 h (For Cu/ZnO/Al₂O₃ catalysts, pretreatments were conducted at 573 K). After the pretreatment, the reactor was cooled down to a target temperature (493–633 K), and was pressurized with a reaction gas mixture (CO₂/H₂/Ar, typically 19/76/5). The outlet gas line was kept at 453 K to prevent condensation of products, and products were analyzed by online gas chromatography (Agilent 8890) equipped with a flame ionization detector (FID) and a thermal conductivity detector (TCD). Agilent HP-PoraplotQ and Restek ShinCarbon were used as columns. Reported data are given as values of time-on-stream at 3 h unless otherwise stated.

Computational studies

The computational approach was based on spin-unpolarized density functional theory within the Perdew-Burke-Ernzerhof⁷⁷ exchange-correlation approximation as implemented in the Vienna Ab initio simulation package (VASP)^{78,79}. The zero-damping D3 correction was added to improve the description of dispersive interactions⁸⁰. To treat strong correlation effects for *d* electrons, the simplified implementation of Hubbard corrections⁸¹ was adopted with U–J = 4 eV on Zr atoms. Atomic charges were assigned using Bader charge analysis^{82,83}. The Gibbs adsorption energies of H were calculated as $G_{ad} = G[\text{H}/\text{cat}] - E[\text{cat}] - 0.5 G[\text{H}_2]$, where $G[\text{H}/\text{cat}]$ is the Gibbs total energy of the system with the adsorbate, while $E[\text{cat}]$ and $G[\text{H}_2]$ are the total and Gibbs total energy of the isolated catalyst model and H₂ molecule in the gas phase. All energetic properties except for the relative energies in Figs. 5b and 6b–d, include Gibbs corrections calculated at 533 K and 4 MPa of H₂ pressure under either the ideal gas or harmonic approximations^{84,85}. In Fig. 6, the H movement coordinate is the quadratic distance of each structure with respect to the corresponding initial state. The *k*-point sampling was performed using Monkhorst-Pack meshes yielding converged adsorption energies of H, namely, the *k*-mesh parameters were 8 × 1 × 1 for all systems containing CNT(5,5), 2 × 2 × 1 for the 10 × 10 supercell of graphene, while the gamma point was sufficient for calculations involving only the ZnZrO_x supercell. All models had a vacuum region of about 11 Å between adjacent slabs and all lateral distances between periodic images were at least 6 Å to keep interactions between periodic images minimal. All systems were optimized with the convergence criteria of 0.03 eV/Å

and 10^{-5} eV for the force on each atom and total electronic energy. To optimize transition states, the climbing image nudged elastic band^{86,87} and dimer⁸⁸ methods were employed and the optimized first-order saddle points were confirmed to have one imaginary vibrational frequency leading to the reported local minima.

Additional details of the methods for catalyst preparation, catalyst characterization, catalytic test, and computational studies are provided in the Supplementary Information.

Data availability

Relevant data supporting the key findings of this study are available within the article and the Supplementary Information file. All raw data generated during the current study are available from the corresponding authors upon request.

References

- Olah, G. A., Goepfert, A. & Prakash, G. K. S. Chemical recycling of carbon dioxide to methanol and dimethyl ether: from greenhouse gas to renewable, environmentally carbon neutral fuels and synthetic hydrocarbons. *J. Org. Chem.* **74**, 487–498 (2009).
- Olah, G. A. Towards oil independence through renewable methanol chemistry. *Angew. Chem. Int. Ed.* **52**, 104–107 (2013).
- Alvarez, A. et al. Challenges in the greener production of formates/formic acid, methanol, and DME by heterogeneously catalyzed CO₂ hydrogenation processes. *Chem. Rev.* **117**, 9804–9838 (2017).
- Jiang, X., Nie, X., Guo, X., Song, C. & Chen, J. G. Recent advances in carbon dioxide hydrogenation to methanol via heterogeneous catalysis. *Chem. Rev.* **120**, 7984–8034 (2020).
- Innovation Outlook: Renewable Methanol. (IRENA AND METHANOL INSTITUTE, International Renewable Energy Agency, 2021).
- Richter, C. *World's First Commercial CO₂ to Methanol Plant*. <https://smartechnology.gatech.edu/handle/1853/61845> (2019).
- Kattel, S., Ramirez, P. J., Chen, J. G., Rodriguez, J. A. & Liu, P. Active sites for CO₂ hydrogenation to methanol on Cu/ZnO catalysts. *Science* **355**, 1296–1299 (2017).
- Zabilskiy, M. et al. The unique interplay between copper and zinc during catalytic carbon dioxide hydrogenation to methanol. *Nat. Commun.* **11**, 2409 (2020).
- Divins, N. J. et al. Operando high-pressure investigation of size-controlled CuZn catalysts for the methanol synthesis reaction. *Nat. Commun.* **12**, 1435 (2021).
- Beck, A. et al. Drastic events and gradual change define the structure of an active copper-zinc-alumina catalyst for methanol synthesis. *Angew. Chem. Int. Ed.* **61**, e202200301 (2022).
- Sun, J. T., Metcalfe, I. S. & Sahibzada, M. Deactivation of Cu/ZnO/Al₂O₃ methanol synthesis catalyst by sintering. *Ind. Eng. Chem. Res.* **38**, 3868–3872 (1999).
- Twigg, M. V. & Spencer, M. S. Deactivation of copper metal catalysts for methanol decomposition, methanol steam reforming and methanol synthesis. *Top. Catal.* **22**, 191–203 (2003).
- Fichtl, M. B. et al. Kinetics of deactivation on Cu/ZnO/Al₂O₃ methanol synthesis catalysts. *Appl. Catal. A Gen.* **502**, 262–270 (2015).
- Liang, B. et al. Investigation on deactivation of Cu/ZnO/Al₂O₃ catalyst for CO₂ hydrogenation to methanol. *Ind. Eng. Chem. Res.* **58**, 9030–9037 (2019).
- Martin, O. et al. Indium oxide as a superior catalyst for methanol synthesis by CO₂ hydrogenation. *Angew. Chem. Int. Ed.* **55**, 6261–6265 (2016).
- Frei, M. S. et al. Role of zirconia in indium oxide-catalyzed CO₂ hydrogenation to methanol. *ACS Catal.* **10**, 1133–1145 (2020).
- Dang, S. et al. Rationally designed indium oxide catalysts for CO₂ hydrogenation to methanol with high activity and selectivity. *Sci. Adv.* **6**, eaaz2060 (2020).
- Wang, J. et al. A highly selective and stable ZnO-ZrO₂ solid solution catalyst for CO₂ hydrogenation to methanol. *Sci. Adv.* **3**, e1701290 (2017).
- Wang, J. et al. High-performance MaZrOx (Ma = Cd, Ga) solid-solution catalysts for CO₂ hydrogenation to methanol. *ACS Catal.* **9**, 10253–10259 (2019).
- Thousand-ton scale demonstration of solar fuel synthesis starts operation in Lanzhou, China. *EurekaAlert* (17 January 2020).
- Frei, M. S. et al. Atomic-scale engineering of indium oxide promotion by palladium for methanol production via CO₂ hydrogenation. *Nat. Commun.* **10**, 3377 (2019).
- Lee, K. et al. Atomic Pd-promoted ZnZrO_x solid solution catalyst for CO₂ hydrogenation to methanol. *Appl. Catal. B Environ.* **304**, 120994 (2022).
- Xu, D., Hong, X. & Liu, G. Highly dispersed metal doping to ZnZr oxide catalyst for CO₂ hydrogenation to methanol: insight into hydrogen spillover. *J. Catal.* **393**, 207–214 (2021).
- Sha, F. et al. The promoting role of Ga in ZnZrOx solid solution catalyst for CO₂ hydrogenation to methanol. *J. Catal.* **404**, 383–392 (2021).
- Huang, C. et al. CO₂ hydrogenation to methanol over PdZnZr solid solution: effects of the PdZn alloy and oxygen vacancy. *ACS Appl. Energy Mater.* **4**, 9258–9266 (2021).
- Behrens, M. et al. The active site of methanol synthesis over Cu/ZnO/Al₂O₃ industrial catalysts. *Science* **6083**, 893–897 (2012).
- Li, S. et al. Tuning the selectivity of catalytic carbon dioxide hydrogenation over iridium/ceria oxide catalysts with a strong metal-support interaction. *Angew. Chem. Int. Ed.* **56**, 10761–10765 (2017).
- Meng, C. et al. Oxygen-deficient metal oxides supported nano-intermetallic InNi₃Co_{0.5} toward efficient CO₂ hydrogenation to methanol. *Sci. Adv.* **7**, eabi6012 (2021).
- Liu, K. et al. Strong metal-support interaction promoted scalable production of thermally stable single-atom catalysts. *Nat. Commun.* **11**, 1263 (2020).
- Parastayev, A. et al. Boosting CO₂ hydrogenation via size-dependent metal-support interactions in cobalt/ceria-based catalysts. *Nat. Catal.* **3**, 526–533 (2020).
- Chen, K. et al. CO₂ hydrogenation to methanol over Cu catalysts supported on La-modified SBA-15: The crucial role of Cu-LaO_x interfaces. *Appl. Catal. B Environ.* **251**, 119–129 (2019).
- Palomino, R. M. et al. Hydrogenation of CO₂ on ZnO/Cu(100) and ZnO/Cu(111) catalysts: role of copper structure and metal-oxide interface in methanol synthesis. *J. Phys. Chem. B* **122**, 794–800 (2018).
- Graciani, J. et al. Highly active copper-ceria and copper-ceria-titania catalysts for methanol synthesis from CO₂. *Science* **345**, 546–550 (2014).
- Rodriguez, J. A. et al. Hydrogenation of CO₂ to methanol: importance of metal-oxide and metal-carbide interfaces in the activation of CO₂. *ACS Catal.* **5**, 6696–6706 (2015).
- Wu, C., Cheng, D., Wang, M. & Ma, D. Understanding and application of strong metal-support interactions in conversion of CO₂ to methanol: a review. *Energy Fuels* **35**, 19012–19023 (2021).
- Zabilskiy, M. et al. Mechanistic study of carbon dioxide hydrogenation over Pd/ZnO-based catalysts: the role of palladium-zinc alloy in selective methanol synthesis. *Angew. Chem. Int. Ed.* **60**, 17053–17059 (2021).
- Li, M. M. et al. Methanol synthesis at a wide range of H₂/CO₂ ratios over a Rh-In bimetallic catalyst. *Angew. Chem. Int. Ed.* **59**, 16039–16046 (2020).
- Wu, C. et al. Inverse ZrO₂/Cu as a highly efficient methanol synthesis catalyst from CO₂ hydrogenation. *Nat. Commun.* **11**, 5767 (2020).

39. Lee, S. M. & Lee, Y. H. Hydrogen storage in single-walled carbon nanotubes. *Appl. Phys. Lett.* **76**, 2877–2879 (2000).
40. Zacharia, R., Rather, S.-U., Hwang, S. W. & Nahm, K. S. Spillover of physisorbed hydrogen from sputter-deposited arrays of platinum nanoparticles to multi-walled carbon nanotubes. *Chem. Phys. Lett.* **434**, 286–291 (2007).
41. Reyhani, A. et al. Hydrogen storage in decorated multiwalled carbon nanotubes by Ca, Co, Fe, Ni, and Pd nanoparticles under ambient conditions. *J. Phys. Chem. C*. **115**, 6994–7001 (2011).
42. Lueking, A. & Yang, R. T. Hydrogen spillover from a metal oxide catalyst onto carbon nanotubes—implications for hydrogen storage. *J. Catal.* **206**, 165–168 (2002).
43. Yoo, E. et al. Atomic hydrogen storage in carbon nanotubes promoted by metal catalysts. *J. Phys. Chem. B* **108**, 18903–18907 (2004).
44. Mu, S.-C., Tang, H.-L., Qian, S.-H., Pan, M. & Yuan, R.-Z. Hydrogen storage in carbon nanotubes modified by microwave plasma etching and Pd decoration. *Carbon* **44**, 762–767 (2006).
45. Briggs, N. M. et al. Identification of active sites on supported metal catalysts with carbon nanotube hydrogen highways. *Nat. Commun.* **9**, 3827 (2018).
46. Hill, A. K. & Torrente-Murciano, L. Low temperature H₂ production from ammonia using ruthenium-based catalysts: synergistic effect of promoter and support. *Appl. Catal. B Environ.* **172–173**, 129–135 (2015).
47. Prins, R. Hydrogen spillover. facts and fiction. *Chem. Rev.* **112**, 2714–2738 (2012).
48. Karim, W. et al. Catalyst support effects on hydrogen spillover. *Nature* **541**, 68–71 (2017).
49. Roland, U., Braunschweig, T. & Roessner, F. On the nature of spilt-over hydrogen. *J. Mol. Catal. A Chem.* **127**, 61–84 (1997).
50. Yu, M.-F. et al. Strength and breaking mechanism of multiwalled carbon nanotubes under tensile load. *Science* **287**, 637–640 (2000).
51. Kumanek, B. & Janas, D. Thermal conductivity of carbon nanotube networks: a review. *J. Mater. Sci.* **54**, 7397–7427 (2019).
52. Diler, E. et al. Initial formation of corrosion products on pure zinc and MgZn₂ examined by XPS. *Corros. Sci.* **79**, 83–88 (2014).
53. Dake, L. S., Baer, D. R. & Zachara, J. M. Auger parameter measurements of zinc compounds relevant to zinc transport in the environment. *Surf. Interface Anal.* **14**, 71–75 (1989).
54. Ruiz Puigdollers, A., Illas, F. & Pacchioni, G. Reduction of hydrogenated ZrO₂ nanoparticles by water desorption. *ACS Omega* **2**, 3878–3885 (2017).
55. Tada, S. et al. Active sites on Zn_xZr_{1-x}O_{2-x} solid solution catalysts for CO₂-to-methanol hydrogenation. *ACS Catal.* **12**, 7748–7759 (2022).
56. Han, E., Fang, W., Stamatakis, M., Richardson, J. O. & Chen, J. Quantum tunnelling driven H₂ formation on graphene. *J. Phys. Chem. Lett.* **13**, 3173–3181 (2022).
57. Burch, R., Golunski, S. E. & Spencer, M. S. The role of copper and zinc oxide in methanol synthesis catalysts. *J. Chem. Soc. Faraday Trans.* **86**, 2683–2691 (1990).
58. Sahibzada, M., Chadwick, D. & Metcalfe, I. S. Hydrogenation of carbon dioxide to methanol over palladium-promoted Cu/ZnO/Al₂O₃ catalysts. *Catal. Today* **29**, 367–372 (1996).
59. Jung, K.-D. & Bell, A. T. Role of hydrogen spillover in methanol synthesis over Cu/ZrO₂. *J. Catal.* **193**, 207–223 (2000).
60. Meliancabrera, I. Pd-modified Cu-Zn catalysts for methanol synthesis from CO₂/H₂ mixtures: catalytic structures and performance. *J. Catal.* **210**, 285–294 (2002).
61. Collins, S. E., Chiavassa, D. L., Bonivardi, A. L. & Baltanás, M. A. Hydrogen spillover in Ga₂O₃-Pd/SiO₂ catalysts for methanol synthesis from CO₂/H₂. *Catal. Lett.* **103**, 83–88 (2005).
62. Liang, X.-L., Dong, X., Lin, G.-D. & Zhang, H.-B. Carbon nanotube-supported Pd-ZnO catalyst for hydrogenation of CO₂ to methanol. *Appl. Catal. B Environ.* **88**, 315–322 (2009).
63. Hu, B. et al. Hydrogen spillover enabled active Cu sites for methanol synthesis from CO₂ hydrogenation over Pd doped CuZn catalysts. *J. Catal.* **359**, 17–26 (2018).
64. Im, J., Shin, H., Jang, H., Kim, H. & Choi, M. Maximizing the catalytic function of hydrogen spillover in platinum-encapsulated aluminosilicates with controlled nanostructures. *Nat. Commun.* **5**, 3370 (2014).
65. Tang, C. et al. Insights into the selectivity determinant and rate-determining step of CO₂ hydrogenation to methanol. *J. Phys. Chem. C*. **126**, 10399–10407 (2022).
66. Zecevic, J., Vanbutsele, G., de Jong, K. P. & Martens, J. A. Nanoscale intimacy in bifunctional catalysts for selective conversion of hydrocarbons. *Nature* **528**, 245–248 (2015).
67. Kasipandi, S. & Bae, J. W. Recent advances in direct synthesis of value-added aromatic chemicals from syngas by cascade reactions over bifunctional catalysts. *Adv. Mater.* **31**, e1803390 (2019).
68. Zhou, W. et al. New horizon in C1 chemistry: breaking the selectivity limitation in transformation of syngas and hydrogenation of CO₂ into hydrocarbon chemicals and fuels. *Chem. Soc. Rev.* **48**, 3193–3228 (2019).
69. Ye, R. P. et al. CO₂ hydrogenation to high-value products via heterogeneous catalysis. *Nat. Commun.* **10**, 5698 (2019).
70. Pan, X., Jiao, F., Miao, D. & Bao, X. Oxide-zeolite-based composite catalyst concept that enables syngas chemistry beyond Fischer-Tropsch synthesis. *Chem. Rev.* **121**, 6588–6609 (2021).
71. Wang, D., Xie, Z., Porosoff, M. D. & Chen, J. G. Recent advances in carbon dioxide hydrogenation to produce olefins and aromatics. *Chem* **7**, 2277–2311 (2021).
72. Liu, S., Kots, P. A., Vance, B. C., Danielson, A. & Vlachos, D. G. Plastic waste to fuels by hydrocracking at mild conditions. *Sci. Adv.* **7**, eabf8283 (2021).
73. Huang, X. et al. Au-Pd separation enhances bimetallic catalysis of alcohol oxidation. *Nature* **603**, 271–275 (2022).
74. Cheng, K. et al. Maximizing noble metal utilization in solid catalysts by control of nanoparticle location. *Science* **377**, 204–208 (2022).
75. Zachopoulos, A. & Heracleous, E. Overcoming the equilibrium barriers of CO₂ hydrogenation to methanol via water sorption: a thermodynamic analysis. *J. CO₂ Util.* **21**, 360–367 (2017).
76. Leonzio, G., Zondervan, E. & Foscolo, P. U. Methanol production by CO₂ hydrogenation: Analysis and simulation of reactor performance. *Int. J. Hydrog. Energy* **44**, 7915–7933 (2019).
77. Perdew, J. P., Burke, K. & Ernzerhof, M. Generalized gradient approximation made simple. *Phys. Rev. Lett.* **77**, 3865 (1996).
78. Kresse, G. & Hafner, J. Ab initio molecular dynamics for open-shell transition metals. *Phys. Rev. B* **48**, 13115 (1993).
79. Kresse, G. & Furthmüller, J. Efficient iterative schemes for ab initio total-energy calculations using a plane-wave basis set. *Phys. Rev. B* **54**, 11169 (1996).
80. Grimme, S., Antony, J., Ehrlich, S. & Krieg, H. A consistent and accurate ab initio parametrization of density functional dispersion correction (DFT-D) for the 94 elements H-Pu. *J. Chem. Phys.* **132**, 154104 (2010).
81. Dudarev, S. L., Botton, G. A., Savrasov, S. Y., Humphreys, C. & Sutton, A. P. Electron-energy-loss spectra and the structural stability of nickel oxide: An LSDA+U study. *Phys. Rev. B* **57**, 1505 (1998).
82. Bader, R. F. The zero-flux surface and the topological and quantum definitions of an atom in a molecule. *Theor. Chem. Acc.* **105**, 276–283 (2001).
83. Henkelman, G., Arnaldsson, A. & Jónsson, H. A fast and robust algorithm for Bader decomposition of charge density. *Comput. Mater. Sci.* **36**, 354–360 (2006).

84. Bahn, S. R. & Jacobsen, K. W. An object-oriented scripting interface to a legacy electronic structure code. *Comput. Sci. Eng.* **4**, 56–66 (2002).
85. Larsen, A. H. et al. The atomic simulation environment—a Python library for working with atoms. *J. Phys. Condens. Matter* **29**, 273002 (2017).
86. Henkelman, G. & Jónsson, H. Improved tangent estimate in the nudged elastic band method for finding minimum energy paths and saddle points. *J. Chem. Phys.* **113**, 9978–9985 (2000).
87. Henkelman, G., Uberuaga, B. P. & Jónsson, H. A climbing image nudged elastic band method for finding saddle points and minimum energy paths. *J. Chem. Phys.* **113**, 9901–9904 (2000).
88. Henkelman, G. & Jónsson, H. A dimer method for finding saddle points on high dimensional potential surfaces using only first derivatives. *J. Chem. Phys.* **111**, 7010–7022 (1999).

Acknowledgements

This work was supported by the National University of Singapore Flagship Green Energy Program (A-0005323-11-00) and the National Research Foundation under the NRF Fellowship NRFF13-2021-0126 and NRF investigatorship NRF-NRF107-2021-0006. Computational work was performed using resources of the National Supercomputing Centre, Singapore. T.-C.Y. and C.-M.Y. gratefully acknowledge the financial support by the Ministry of Science and Technology, Taiwan under contract No. MOST 109-2113-M-007-018-MY3 and MOST 111-2634-F-007-007 and by the Frontier Research Center on Fundamental and Applied Sciences of Matters from The Featured Areas Research Center Program within the framework of the Higher Education Sprout Project by the Ministry of Education (MOE) in Taiwan. Ms. Wang Zhan for the quasi in situ XPS experiment.

Author contributions

K.L. and N.Y. conceived the project. N.Y. supervised the project and revised the manuscript. K.L. carried out most experiments, conducted data analysis, and drafted the initial manuscript. M.P.D. participated in catalyst synthesis and reaction testing. P.C.D.M., Y.S., and U.A. conducted DFT calculations and analyses, prepared the DFT draft, and revised the manuscript, P.C.D.M. also wrote the computer scripts, oversaw the methodology and draft for the DFT part, S.M.K. conceptualized, supervised, revised the draft and manuscript, and conducted data analysis for the DFT part. H.J. and M.C. conducted and

analyzed H₂/CO chemisorption, CO₂-TPD, H₂-TPD, and H₂-D₂ exchange experiments. L.C., K.L., and N.Y. conducted XPS experiments and analyzed data. T.-C.Y. and C.-M.Y. conducted and analyzed XAFS experiments. All authors participated in the discussions, commented, and edited the manuscript.

Competing interests

The authors declare no competing interests.

Additional information

Supplementary information The online version contains supplementary material available at <https://doi.org/10.1038/s41467-023-36407-1>.

Correspondence and requests for materials should be addressed to Sergey M. Kozlov or Ning Yan.

Peer review information *Nature Communications* thanks the anonymous reviewers for their contribution to the peer review of this work.

Reprints and permissions information is available at <http://www.nature.com/reprints>

Publisher's note Springer Nature remains neutral with regard to jurisdictional claims in published maps and institutional affiliations.

Open Access This article is licensed under a Creative Commons Attribution 4.0 International License, which permits use, sharing, adaptation, distribution and reproduction in any medium or format, as long as you give appropriate credit to the original author(s) and the source, provide a link to the Creative Commons license, and indicate if changes were made. The images or other third party material in this article are included in the article's Creative Commons license, unless indicated otherwise in a credit line to the material. If material is not included in the article's Creative Commons license and your intended use is not permitted by statutory regulation or exceeds the permitted use, you will need to obtain permission directly from the copyright holder. To view a copy of this license, visit <http://creativecommons.org/licenses/by/4.0/>.

© The Author(s) 2023